Elasto-capillary deformations of films and rods

ELASTO-CAPILLARY DEFORMATIONS OF FILMS AND RODS

BY

ADAM FORTAIS, B.Sc.

A THESIS

SUBMITTED TO THE DEPARTMENT OF PHYSICS & ASTRONOMY

AND THE SCHOOL OF GRADUATE STUDIES

OF MCMASTER UNIVERSITY

IN PARTIAL FULFILMENT OF THE REQUIREMENTS

FOR THE DEGREE OF

MASTER OF SCIENCE

Master of Science (2016) McMaster University

(Physics & Astronomy) Hamilton, Ontario, Canada

TITLE:	Elasto-capillary deformations of films and rods
AUTHOR:	Adam Fortais B.Sc., (Physics & Astronomy) Western University, London, Canada
SUPERVISOR:	Dr. Kari Dalnoki-Veress
NUMBER OF PAGES:	ix, 60

Abstract

Elasto-capillarity is the ability of capillary forces to deform elastic structures. This phenomenon is found at all length scales and is central to natural phenomena such as the coalescence of wet hairs as well as technological applications like microfluidics and microelectromechanical systems. In this thesis we investigate some of the most fundamental examples of elasto-capillarity – the deformation of thin films and rods by liquid drops and bubbles. Through novel experiment techniques we are able to accurately predict the shape of elastic deformations in compliant polymer films as a function of tension in the film due to capillary forces from liquid drops. We are also able to accurately predict the onset of winding of slender polymer rods around liquid bubbles.

Contents

List of Figures

Acknowledgements

I remember Kari telling a story about one of the first times he had even met de Gennes. I particularly remember how animated Kari got recalling the excitement of being noticed and – can you believe it, even complimented by! – P-GG. It was clear this was an experience that he was truly shaped by. Receiving praise and support from someone you admire and knowing they truly mean it... after the last two years in Kari's group I'd like to think that maybe I can relate to that.

I don't think the hard part is *finishing* the Master's program. The hard part comes in realizing an M.Sc is exactly what you make it, and there are no bounds on what can be accomplished. Kari provided me with all the support and guidance I could ask for (plus that little push to surprise even myself). This is the best I can do to try and distill 2 years worth of thank-yous into 1 page. I had a lot more to say. I'll save it for Ph.D. Thank you so much, Kari.

But enough about Kari, have you met his group? It is truly a pleasure coming in to the lab every day, if not for the expertise (scientific all-stars) then for the fun! Raffi, Paul, Mark, BDP, Solomon, JC, John, beers after I defend this thing? And finally, friends, family, Sarah? There are a HUGE number of hours I didn't spend in the lab, and a guy needs support out there too. I hopefully make my appreciation clear day to day, but if I don't, here it is in writing. Thank you. I love you all.

Chapter 1

Introduction

The natural world is full of systems composed of solids and liquids whose characteristics are determined by the interaction between these phases. From the viscous drag which slowly carves rivers into the Earth to blood-flow due to the hydrostatic pressure caused by the contraction of your heart, solid-liquid interactions are at the core of many fundamental phenomena. While many examples of solid-fluid interaction happen on large scales and are typically described by the fluid's weight or flow, the continued development of micro-sized devices requires the understanding interfacial tension and how a liquid wets a solid.

Wetting of liquids on solids is ubiquitous and can be found in a wide variety of natural and industrial phenomena such as coalescence and deformation of wet hairs and fibers [1–4], drying of textiles [5], and spreading of liquids on surfaces [6–8], among many other examples [9]. Wetting phenomena such as these are a result of the interaction of two phases at an interface. As the size of the system decreases, the surface area decreases much slower than the volume does. This increases the relative magnitude of interfacial tension-based effects compared to effects which scale

with volume like gravity or some elastic deformations. In fact, as the scale of a system decreases, interfacial tension effects may become more dominant than typically much stronger effects like gravity and elasticity. In particular, the subject of elasto-capillarity aims to understand phenomena resulting from the competition between elasticity and interfacial tension. Elasto-capillary interactions are relevant in a wide variety of systems including capillary folding (capillary origami) [2, 10–12], wetting of fibers, soft tissues [13–15], and micropatterning of elastomeric surfaces [16–18].

While elasto-capillary phenomena are being used in technological applications today, many fundamental questions still remain. This thesis investigates how the interfacial tension between a liquid and elastic solid can deform the solid. In Chapter 1, interfacial tension, elasticity and elasto-capillarity as they relate the presented work are discussed. Chapter 2 discusses details of the experiments in the proceeding chapters. In Chapter 3 liquid drops are found to deform a free-standing thin elastic film. The contact angle the drop makes with the film and the deformation in the film due to the drop are studied as the tension in the film changes. In Chapter 4, the way an elastic fiber can be deformed and subsequently wrap around a liquid membrane-like bubble is explored.

1.1 Interfacial Tension

At material interfaces, interfacial tension results from the cohesive forces between like-molecules [19]. Considering a liquid in contact with air, this cohesive force provides a tension at the surface of the fluid which is tangent to the surface of the fluid. The interfacial tension between liquid and air is called surface tension and creates a tendency for the fluid to minimize its surface area under the constraint of constant

volume. Interfacial tension has dimensions of force per unit length, or equivalently, energy per unit area. In this sense, one can think of interfacial tension as an energy cost to create additional surface area. One of the effects of the tendency to minimize surface area is the Laplace pressure.

1.1.1 Laplace Pressure

The Laplace pressure is the pressure difference between the inside and the outside of a curved surface and is a result of interfacial tension. An illustrative example of the consequences of Laplace pressure is found by considering the shape of a liquid drop in air. Ignoring external forces like gravity, it is intuitive that a drop will form a sphere. This is because the cohesive forces between the molecules which make up the liquid are attractive, which leads to the drop reducing the amount of surface area in contact with the surrounding air. For a given volume, forming a sphere minimizes its surface area. Maintaining a constant volume requires outward-facing pressure inside the drop to balance the tendency to reduce surface area. This pressure is known as the Laplace pressure. The magnitude of the Laplace pressure can be calculated by performing a horizontal force balance around the equator of a drop, of which one hemisphere is shown in Figure 1.1 [19].

The tension in the horizontal plane can be balanced by the pressure acting in the horizontal direction by considering the pressure that acts on the cross-sectional area. The force in the horizontal direction due to pressure is then; $F_p = P_L \pi R^2$ where P_L is the Laplace pressure, and R is the radius of our drop. Calculating the force due to surface tension around the hemisphere F_γ (which is in the horizontal direction and scales with the circumference of the hemisphere) gives $F_\gamma = \gamma 2\pi R$, where γ is the

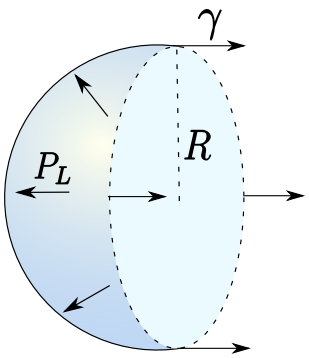

Figure 1.1: Schematic of one hemisphere of a liquid drop with radius R in air. Forces due to the Laplace pressure P_L within the left hemisphere and surface tension around the hemisphere γ are depicted with arrows.

surface tension between the drop material and air. The result of the this force balance is,

$$\begin{aligned} F_L &= F_\gamma \\ P_L \pi R^2 &= \gamma 2\pi R \\ P_L &= \frac{2\gamma}{R}. \end{aligned} \tag{1.1}$$

Laplace pressure is an important parameter in the study of drops and bubbles. For example, a drop which is sessile on a surface applies a force into the surface proportional to the drop's Laplace pressure which can be relevant when drops partially wet deformable surfaces.

1.1.2 Partial Wetting and the Capillary Length

A simple example of partial wetting occurs when a liquid drop contacts the surface of an infinitely rigid solid. Provided the liquid does not spread to cover the whole surface and gravity can be ignored, the drop will form a familiar spherical cap geometry with a contact angle θ_y, known as Young's angle [20]. This is shown in Figure 1.2. To assess the significance of gravity the size of the drop can be compared to the capillary length $L_{\mathrm{GC}} = \sqrt{\gamma/\rho g}$ where ρ is the density of the liquid and g is the gravitational acceleration [19]. L_{GC} is a characteristic length scale which compares the significance of gravity and surface tension. For a drop smaller than L_{GC} sessile on a rigid surface, interfacial tension effects are larger than gravity effects and the drop will form a spherical cap. For clean water and air at room temperature, $L_{\mathrm{GC}} \approx 2\mathrm{mm}$.

A liquid drop below L_{GC} which partially wets a rigid surface has three interfacial tensions which completely define the shape the liquid drop makes with the solid surface. The solid-vapor, γ_{sv}, liquid-vapor, γ, and solid-liquid γ_{sl} interfacial tensions which are shown in Figure 1.2 (A), and can be balanced at the contact line. The Laplace pressure in the drop applies a force into the solid. However, assuming the solid is rigid and the deformation of the solid is negligible, the contact angle can be found by balancing the interfacial tensions in the horizontal direction,

$$\begin{aligned} \gamma\cos(\theta_y) &= \gamma_{sv} - \gamma_{sl} \\ \theta_y &= \cos^{-1}\left(\frac{\gamma_{sv} - \gamma_{sl}}{\gamma}\right). \end{aligned} \tag{1.2}$$

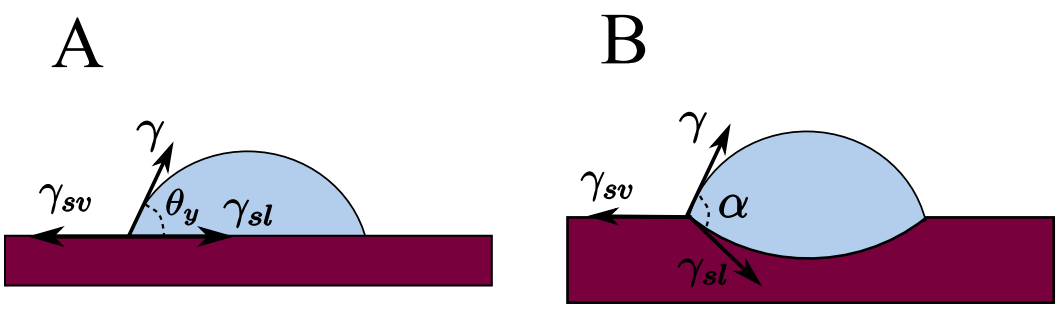

Figure 1.2: Liquid drop partially wetting an undeformable solid surface (A) and a completely deformable liquid surface (B). Interfacial tensions are represented with arrows.

If a liquid drop now rests on a deformable surface like another liquid, the underlying surface will deform due to the drop's Laplace pressure creating an interior angle α. An example of this is a drop of oil floating on water, and a schematic of such a system is shown in Figure 1.2 (B). Again, for systems below L_{GC}, the shape of the drop is completely determined by balancing the interfacial tensions at the contact line. However, to solve for α the vertical as well as the horizontal interfacial tension components must be balanced. This is known as a Neumann construction.

The extreme cases of partial wetting on rigid solids and liquids have been studied extensively and are fairly well understood. However, the intermediate case of a liquid drop wetting a deformable solid surface has garnered much attention recently [17, 21–30]. The specifics of deformations in the case of an elastic surface can be complicated and are exemplary of the problems within the field of elasto-capillarity.

1.2 Elasto-Capillarity

Elasto-capillary phenomena occur when elastic forces and capillary forces compete on similar length scales. In the example of a liquid drop partially wetting a solid surface, capillary forces at the interface attempt to deform the solid surface. However, the high Young's modulus E or stiffness of most solids means any deformations will be extremely small. However looking at various length scales and geometries, one can observe a rich variety of phenomena. Likewise, dealing with soft materials like gels may also amplify these deformations [17, 21–30]. Figure 1.3 shows examples of the type of deformations one may observe due to elasto-capillary effects at various length scales. In all cases pictured, the system is far below L_{GC} and the solid material deforms under the liquid drop due to the Laplace pressure in the drop. In Figure 1.3 (A) and (B), a liquid drop rests atop a thin, compliant film and undergoes a uniform bending where tension in the film defines the morphology. Closer to the interface between drop and film, Figure 1.3 (C) schematically shows a length-scale which is defined by the bending energy [2, 23, 31]. This is called the bending elasto-capillary length, L_{BC}. Finally, a distinct cusp-like shape is shown in Figure 1.3 (D) which demonstrates yet another length scale – the elasto-capillary length L_{EC} – defined by the bulk elasticity of the solid [22, 25]. These different length scales will be considered from small to large.

1.2.1 Bulk Elasticity and the Elasto-Capillary Length

The elasto-capillary length L_{EC} determines the length scale over which elastic effects are comparable to capillary effects. An elastic structure will exhibit significant deformation when the reduction of interfacial energy during elastic deformation is comparable to the energetic cost of such a deformation. For example, consider the

cusp in Figure 1.3 (D). The vertical component of surface tension is $\gamma\sin(\theta_d)$ which pulls the elastic material upwards, forming a cusp. If δ is the height of the resulting cusp above the undeformed surface, the elastic force per unit length is of order $E\delta$ where E is the elastic modulus of the material. The vertical surface tension component must be proportional to the elastic force per unit length, and from this the length scale of the elastic deformation in the solid can be determined;

$$\begin{aligned} \gamma\sin(\theta_d) &\sim E\delta \\ \delta &\propto \frac{\gamma\sin(\theta_d)}{E}, \end{aligned} \tag{1.3}$$

and from this, the elasto-capillary length can be defined, $L_{\mathrm{EC}} = \frac{\gamma}{E}$. Comparing typical values for a soft, gel-like solid ($E_{\mathrm{gel}} \sim 1$ MPa) and a glassy polymer ($E_{\mathrm{glass}} \sim$ GPa) deformed by a glycerol drop ($\gamma = 64$ mN/m), the elasto-capillary lengths are $L_{\mathrm{EC}} \sim 10$ nm and $L_{\mathrm{EC}} \sim 10$ pm respectively. For a soft material like a gel, this length scale is not out of reach of current technologies and can be relevant in biological systems but the length scale of deformation in a typical glassy polymer is of atomic scale.

1.2.2 The Bending Elasto-Capillary Length of Films and Slender Rods

At length scales larger than L_{EC}, one reaches the bending elasto-capillary length L_{BC}. L_{BC} is the length scale over which bending energy becomes dominant. Up until this point, a system consisting of a drop wetting a thin film has been considered. We now turn to the case of a liquid drop partially wetting a thin rod as its calculation which

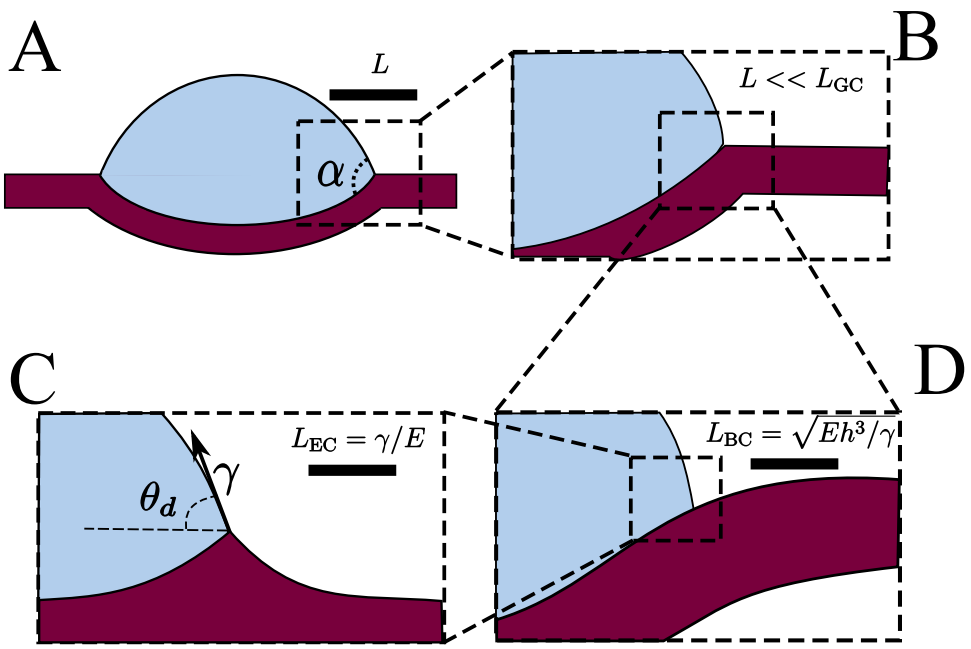

Figure 1.3: Example of two elasto-capillary phenomena. (A) A liquid drop deforms a soft solid and creates a cusp at the contact line which has a length scale defined by the system's elasto-capillary length. (B) A liquid drop deforms a high modulus yet thin, compliant solid creating a bulge in the solid. The cusp in (B) is much smaller than in (A) since the elasto-capillary length in the stiff system is much shorter than in the soft system.

is used directly in Chapter 4.

A thin, deformable rod partially wet by a spherical liquid drop is shown schematically in Figure 1.4. The energetic cost of deforming the rod around the drop competes against the reduction in interfacial energy by the increase of interfacial area between the rod and drop. By balancing these contributions a threshold for which it is expected that the rod will spontaneously wrap around the drop can be determined, and from this, a characteristic length scale can be defined. The interfacial and bending energies will be calculated in turn.

If the solid rod and a liquid sphere do not begin in contact with one another, each object will have a interfacial energy equal to the object's surface area multiplied by its surface tension. Once the rod and drop make contact, the rod may deform to increase its total area in contact with the drop, A. Call $A = \kappa r l$ the contact area, where l is the length of rod in contact with the drop, r is the radius of the rod, and κ is a dimensionless geometric factor relating r to the area of the rod in contact with the drop. The liquid drop has then replaced an area A in contact with vapor with an area A in contact with the rod. Likewise, the rod has lost an interfacial area A in contact with vapor and replaced it with an area A in contact with the drop. Assuming κr is constant with respect to l the change in interfacial energy ΔE_{surf} is then,

$$\Delta E_{\text{surf}} = \kappa r l(\gamma_{sl}) - L\kappa r(\gamma_{sv} + \gamma), \tag{1.4}$$

where γ, γ_{sl} and γ_{sv} are liquid-vapor, solid-liquid and solid-vapor interfacial tensions. Using Young's law from Equation 1.2 to obtain the change in interfacial energy per unit length of rod in contact with the drop,

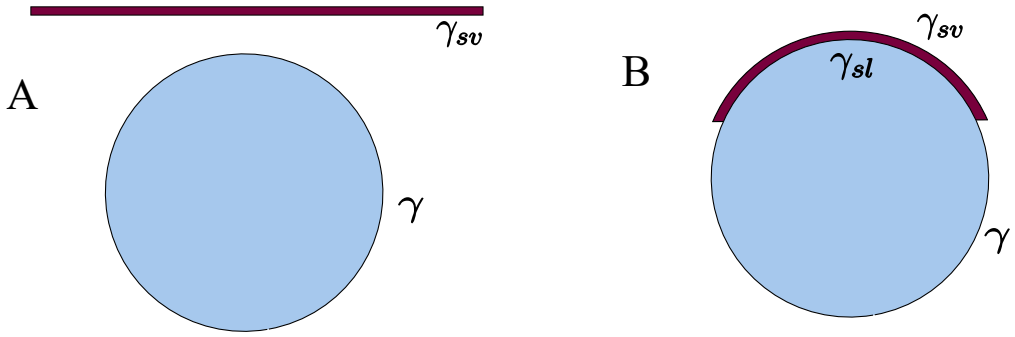

Figure 1.4: A liquid drop and flexible solid rod before (A) and after (B) making contact with each other. The liquid drop partially wets the rod, elastically deforming the rod around the circumference of the drop. Solid-liquid, liquid-vapor and solid-vapor interfaces are labeled with their interfacial tensions γ, γ_{sv}, and γ_{sl}.

$$\Delta E_{\text{surf}}/l = \kappa r(1 - \cos(\theta_y)). \tag{1.5}$$

For a sufficiently thin rod undergoing small deformations, assume the bending occurs in a single plane, and the internal stresses come from stretching and compression [32]. That is, approximate the bending of the rod as stretching or compression of every volume element within our thin rod. Therefore, the bending energy E_{bend} can be solved by finding the free energy $\frac{1}{2}\sigma_i\epsilon_i$ for each volume element, where σ_i is the stress in element i, and ϵ_i is the strain. For small deformations, assume linear elasticity such that $\sigma = E\epsilon$ where E is the elastic modulus of the rod material. This gives a free energy per volume element,

$$E_{\text{bend},i} = \frac{E\epsilon_i^2}{2}. \tag{1.6}$$

The strain is calculated by identifying a neutral surface parallel to the length of our rod which undergoes no stretching or compression. For a cylindrical rod, this passes through the centre of mass [32]. Taking a surface parallel to the neutral surface but displaced above or below it, bend the rod uniformly across its length. This new surface will exhibit a strain which can be calculated considering the surface to be an arc of constant curvature and comparing its arc length with respect to the arc length of the neutral surface. Calculating a unit of arc length $\mathrm{d}z'$ displaced x above the neutral surface,

$$\mathrm{d}z' = \frac{R+x}{R}\,\mathrm{d}z = (1+\frac{x}{R})\,\mathrm{d}z, \tag{1.7}$$

where $\mathrm{d}z$ is a a unit of arc length of the neutral surface and R is the radius of curvature of the neutral surface. Therefore the strain is,

$$\epsilon = \frac{\mathrm{d}z' - \mathrm{d}z}{\mathrm{d}z} = \frac{x}{R}. \tag{1.8}$$

To find E_{bend} per unit length we substitute Equation 1.8 into Equation 1.6 and integrate over the cross-sectional area of the rod which again we take to be circular,

$$\begin{aligned}\frac{\Delta E_{\text{bend}}}{L} &= \int \frac{E\epsilon_i^2}{2}\mathrm{d}Av = \int \frac{Ex^2}{2R^2}\mathrm{d}A \\ &= \frac{EI}{2R^2} = \frac{E\pi r^4}{8R^2},\end{aligned} \tag{1.9}$$

where $I = \int x^2 \, \mathrm{d}A = \frac{\pi r^4}{4}$ is the moment of inertia of the cross-section. Setting Equation 1.9 equal to Equation 1.5,

$$\frac{E\pi r^4}{8R^2} = \kappa r\gamma(1 - \cos(\theta_y)). \tag{1.10}$$

Re-arranging, we find $R \propto \sqrt{\frac{Er^3}{\gamma}}$. R is the radius of curvature of the rod which is a result of the minimization of interfacial energy between the rod and drop. If the radius of the drop is roughly equal to R one would expect to observe significant deformation in the rod. Therefore, we define the bending elasto-capillary length, $L_{\text{BC}} = \sqrt{\frac{Er^3}{\gamma}}$. Chapter 4 involves a polymer fiber deforming in a similar manner around a liquid bubble of radius $\sim L_{BC}$.

Returning to a thin film deformed by a drop with radius $> L_{BC}$, one would expect a bending-dominated morphology at length scales $\propto L_{BC}$ as shown in Figure 1.3 (C). However, at lengths $> L_{BC}$ forces related to bending are expected to be small compared to the tension in the film. Because of this, a liquid drop can readily deform the underlying film, resulting in a morphology that can be determined by considering the tension in the film.

Considering $\Gamma, \gamma, \gamma_{sv}$, and γ_{sl} at the contact line, a Neumann construction can be made, just as was done above in the case of a liquid partially wetting a liquid. The

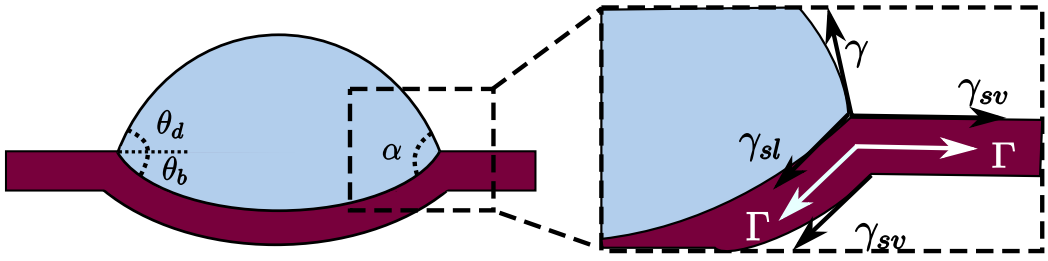

Figure 1.5: A liquid drop partially wetting a compliant solid film. The interior angle of the drop α is shown, which is divided into a drop θ_d and bulge θ_b contant angle. The contact line is shown with interfacial tensions γ, γ_{sv}, and γ_{sl} and elastic tension Γ.

interior angle α us divided into two angles, $\alpha = \theta_d + \theta_b$ where θ_d is the angle the drop makes with the undeformed solid, and θ_b is the angle the bulge in the film makes with the undeformed film as shown in Figure 1.5. Performing a vertical tension balance,

$$\begin{aligned} \gamma\cos(\theta_d) &= (\gamma_{sv} + \gamma_{sl} + \Gamma)\cos(\theta_b) \\ \frac{\cos(\theta_d)}{\cos(\theta_b)} &= \frac{\gamma_{sv} + \gamma_{sl} + \Gamma}{\gamma}. \end{aligned} \tag{1.11}$$

Under the assumption that the drop has a radius $L_{\mathrm{BC}} < R < L_{GC}$, the drop and bulge will take on the shape of spherical caps at macroscopic length scales. By solving for the interior angle of the drop, the shape of the deformation can be completely determined. Comparing this result to a liquid partially wetting another liquid, a drop partially wetting a deformable solid should converge to the liquid-liquid case as $\Gamma \to 0$.

Chapter 2

Experimental Details

This chapter describes in detail the experiments which follow in Chapter 3 and Chapter 4. All of the following experiments are performed on scales similar to that of dust particles. As such, cleanliness is of the utmost importance. Additionally, the following experiments depend on the interfacial tensions of various materials. Contamination can cause significant changes in surface properties of materials, so it is important that samples be pure and uncontaminated. Whenever possible, samples preparation took place in a laminar flow hood and samples were used as soon after production as possible.

2.1 Spincoating

Chapter 3 involves the deformation of thin, free-standing films by sessile liquid drops. The films were produced through the spincoating process. In this process, polymer is dissolved in a volatile solvent and and the solution is placed on a substrate. Both the solvent and solution are filtered with 0.2 mm Milipore filters (Millex). The substrate is

rotated at high speeds, producing a thin, uniform layer of solution. As the substrate rotates, solvent evaporates from solution leaving behind a thin, uniform film. By adjusted the spin speed and concentration of solution, the thickness of a resulting film can range from several nm to several μm. For example, samples in Chapter 3 were made from several polystyrene (PS) solutions with molecular weight $M_n = 451,000$ kg/mol and PDI = 1.10 (Polymer Source Inc.). PS was dissolved in toluene (Fisher Scientific, Optima grade) with concentrations ranging from 0.5-2%. The solution was spin cast on to freshly cleaved mica films (Ted Pella Inc.) at speeds between 1000-4000 rpm resulting in films of uniform thicknesses between 30-110 nm. After spincoating, the polymer film could be divided into several usable films by scoring the film with a scalpel. Typically 4 samples were made from a single polymer film.

2.2 Substrates

Three substrates were used to prepare samples in Chapter 3. Polymer solutions were spin cast on mica films. Mica films were cleaved by separating two layers of mica with a scalpel. By carefully pulling these layers apart, a large, clean, atomically flat surface can be prepared. Silicon (Si) wafers were used as substrates while measuring the thickness of polymer films. The films were water-transfered from mica on to roughly 1 cm squares of Si with a $\approx$ 5 nm native oxide layer. To produce these small Si squares, large Si wafers are cleaved along the (100) crystallographic planes after which nitrogen gas is blown across the surface to remove any Si dust produced from cleaving. Free-standing films were prepared by water-transferring polymer films from mica to 1 cm x 1 cm steel washers with 3 mm diameter circular holes. The water-transfer process is detailed below.

2.3 Annealing

Before water-transferring polymer films from mica to another substrate, the films were vacuum annealed for a minimum of 12 hours at 130 °C (above the glass transition temperature of PS) to remove any remaining solvent trapped in the film as well as relax any internal stress or polymer-alignment caused by shear forces induced through spincoating. This is an important step as internal stress and polymer-alignment may affect polymer properties like surface energy. Additionally, trapped solvent may act as a plasticizing agent in the polymer, reducing the glass transition temperature. By heating above the glass transition temperature, the polymer becomes fluid allowing polymer chains to re-orient and release trapped solvent.

Samples which had been water-transferred to steel washers were annealed again at 102 °C for 2 minutes on a hot stage (Linkam) to relax any pre-tension and remove wrinkles which may have formed during the transfer process. This process takes different lengths of time for different samples, however 2 minutes was found to be enough time to relax wrinkles in the slowest to relax films without having the film rupture. The steel washer has a much lower thermal expansion coefficient than PS so cooling the sample results in an isotropic tension in the film due to differential expansion between the washer and the film, similar to the tensioning of a drum head.

2.4 Preparation of Free-standing and Supported Films via Water Transfer

Polymer films on a mica substrate which has been scored could be transferred to different substrates by floating the films on the surface of an ultra-pure water bath

(18.2 MΩ·cm) and picking them up again with the new substrate. Since water has a greater affinity for mica than PS, the water will displace the PS film, leaving the film floating on the surface of the bath. Films were then picked up from under the surface of the bath with either a Si substrate or steel washer, resulting in a supported polymer film or a free-standing polymer film respectively. After water-transferring, samples were allowed to dry for 15-20 minutes.

2.5 Measuring Polymer Film Thickness via Ellipsometry

Ellipsometry is a technique that can be used to determine the thickness and polarization of polymer films, and is the technique used in Chapter 3. After dividing a polymer film on mica into several smaller films, one of these sections was water-transferred on to a 1 cm x 1 cm Si square. This produced a supported polymer sample with which ellipsometry (Accuron EP3) could be performed. The basic principle of ellipsometry is straightforward, though the analysis of the results is more involved [33]. A laser provides linearly polarized monochromatic light directed towards a thin film sample. The laser is first passed through a quarter-wave plate to create circularly polarized light. Then the beam passes through the first polarizer to fix the polarization which is now approximately the same intensity in any orientation of the polarizer because of the first quarter-wave plate. The beam passes through a second quarter-wave plate to produce light of a unique ellipticity. Now, when elliptically polarized light is reflected from the thin film sample it will become linearly polarized. The beam then passes through another polarizer – the analyzer – before reaching the detector. During this

process, the polarizers can be rotated to obtain a minimum in the intensity at the detector. Information about the angle of the polarizers can be used to determine the thickness and refractive index of the sample [33].

2.6 Micropipettes

Micropipettes are used in Chapter 3 and Chapter 4 for two distinct purposes. In Chapter 3, micropipettes are used to place micron-sized liquid drops on the polymer films described above. In Chapter 4, micropipettes are used to pull polymer fibers from polymer melts. The preparation and use of these micropipetttes are discussed below.

2.6.1 Fabrication

Micropipettes are made by stretching glass capillary tubes with an inner diameter of 0.7 mm and outer diameter of 1.0 mm (World Precision Instruments Inc.) with a pipette puller (Narishige PN-30) over a hot filament. This results in pipettes with ends with an inner diameter of $\sim$ 10 μm and an outer diameter of $\sim$ 20 μm. The length of the thin end is approximately 2-4 cm long but can be snipped to a shorter length.

2.6.2 Droplet Production

Micron-sized liquid drops are produced by dipping the thin end of a micropipette into a liquid and rapidly pulling it out. A thin layer of fluid coats the end of the micropipette before dewetting into several micron-sized droplets. Droplets can be

flicked from the micropipette, or gently placed, onto a new surface. Placing droplets on to a free-standing polymer film can be difficult as films are typically very delicate. Flicking has the advantage that the micropipette never comes more than ∼1 cm from the film, reducing the risk of damaging the film with the micropipette.

2.6.3 Polymer Fiber Production

Polymer fibers with micron-sized radii were also produced using micropipettes. Fibers were made from several different polymers, requiring slightly different fiber production techniques. PS (Mn = 25000 kg/mol, PDI = 1.04, Polymer Source Inc.) and Elastollan 1185A 10 (BSF Inc.) fibers were made by dipping a micropipette into the polymer which was supported on a Si wafer held at 170 ^{o}C and 235 ^{o}C respectively via hot stage. The micropipette was then quickly pulled out of the polymer. This resulted in fibers with radii 1 μm $< r <$ 10 μm, as measured by optical microscopy. Fibers of similar dimensions were made from styrene-isoprene-styrene (SIS) by dipping a micropipette into a viscous solution of the polymer dissolved in toluene supported on a Si wafer and quickly pulling the pipette out. In both cases a long, thin polymer fiber was produced with uniform radii over $\sim$ 1 cm length scales.

Chapter 3

Deformation of Thin Free-standing Films with Sessile Droplets Through the Glass Transition

3.1 Preamble

The following chapter contains a manuscript intended for a peer-reviewed publication. It is an extension to the work of R. D. Schulman and K. Dalnoki-Veress which was published in Physical Review Letters in 2015 [29]. In their work, the contact angle of a drop which partially wets thin, deformable, free-standing films is considered, and a minimal model is developed which accurately predicts the contact angle as a function of interfacial and elastic tensions in the film. In the following manuscript, this model is tested in glassy polymer films, where the tension is modulated within a single experiment via temperature. It is found that the model continues to accurately predict the contact angles between drop and film over a wide range of elastic tensions,

even through the glass transition temperature where the polymer film becomes liquid and tension becomes zero. This chapter confirms the minimal model presented by Schulman and Dalnoki-Veress is sufficient for describing elasto-capillary deformations in films in the membrane limit where deformations in the film by liquid droplets are perturbative to the total area of the film. This chapter also demonstrates the robustness of the tension measuring technique presented by Schulman and Dalnoki-Veress.

I designed and performed all experiments, data analysis, and wrote the following manuscript in collaboration with my coauthors Schulman and Dalnoki-Veress.

3.2 Introduction

Elasto-capillarity; the interplay between interfacial tension and elasticity, is of fundamental importance in many active areas of research including microfluidics [34], self-assembly [2, 10, 31, 35, 36], substrate patterning [16, 18, 21], wetting of fibers [1, 3, 37–39], and biological systems [13–15]. With such a wide range of applications, a fundamental aspect of these systems – the contact angle a liquid drop makes with a soft solid – has garnered a great deal of interest [17, 21–30].

Partial wetting of a liquid on a hard solid and partial wetting of a liquid on a liquid are well understood [19]. Below the capillary length L_{GC} gravity can be ignored and a liquid drop which is supported by an undeformable solid substrate will form a spherical cap. The spherical cap will exhibit a contact angle which can be calculated by performing a horizontal interfacial tension balance, which is known as Young's law [20]. Forces in the vertical direction are compensated by the elasticity of the substrate. On a liquid substrate, the Laplace pressure of the droplet is able

to deform the underlying liquid. The construction of a Neumann triangle in which the vertical and horizontal components of the interfacial tensions are simultaneously balanced allows one to determine the interior angle formed between the two liquids [19]. For intermediate systems where substrates are soft, the droplet deforms the substrate at the contact line into a cusp with a length scale comparable to L_{EC} for bulk deformation γ/E where γ is surface tension and E is the elastic modulus [21, 23, 25, 26, 40]. Microscopically, the contact angle between drop and substrate cusp satisfy a Neumann construction balancing the interfacial tension of the liquid and surface stresses between solid-liquid and solid-vapor interfaces. Macroscopically, the contact angle a drop larger than γ/E makes with the planar, undeformed film satisfies Young's law [17, 22, 24, 30]. However, for drops smaller than γ/E these contact angles deviate from Young's law [17].

In order to observe micron-scale deformations in the substrate, experiments are typically limited to soft materials with E in the kPa range such that the elasto-capillary length L_{EC} is on the order of microns. Alternatively, stiff but compliant materials (ie. thin, free-standing films similar to a taut drum head with E on the order of GPa) having sub-nanometer values of L_{EC} may still exhibit macroscopic deformations with length scales greater than the bending elasto-capillary length L_{BC} of the substrate [28, 29, 41].

In this chapter the contact angles between liquid drops on thin, deformable films ($E \sim$ GPa) as a function of film tension are studied. Tension is modulated via film thickness and temperature, and contact angles are measured continuously from well below the glass transition T_g of the film, into the melt state. A Neumann construction is developed and found to accurately predict the contact angle made between drops

and the film, from the high tension regime where the system approaches partial wetting on a rigid solid, into the melt state where the system becomes partial wetting between two liquids. With these measurements, the elastic modulus of our film can also be determined.

3.3 Experiment

Polystyrene (PS) with molecular weight $M_n = 451,000$ kg/mol and polydispersity PDI = 1.10 (Polymer Source Inc.) was dissolved in toluene (Fisher Scientific, Optima grade) and spin cast on to freshly cleaved mica films (Ted Pella Inc.) creating films with uniform thicknesses between 30-110 nm. The samples were vacuum annealed for a minimum of 12 hours at 130 °C. After cooling to room temperature, films were cut into several smaller films and floated on the surface of an ultra-pure water bath (18.2 MΩ·cm), then transferred to 1 cm x 1 cm steel washers with a 3 mm diameter circular hole, producing free-standing films. Additionally, one film from each sample was transferred to a silicon wafer for its thickness to be measured via ellipsometry (Accurion, EP3).

The samples were placed in the experimental set-up shown schematically in Figure 3.1 (A) and pre-annealed at 102 °C for 2 minutes to relax any pre-tension and remove wrinkles which may have formed from transferring the film to the washer. The sample was quenched to 70 °C creating a taut film with uniform tension. Glycerol (Caledon Laboratories Ltd.) drops were deposited on either side of the films. In this way, both liquid drops on the top side and the deformations in the film due to drops (bulges) could be imaged simultaneously from the side using an optical microscope. This is shown schematically in Figure 3.1 (B). The size and number of drops deposited

were limited to contact radii between 25-100 μm, covering a combined contact area $<$ 5% of the film. The lower limit was imposed to reduce the effects of evaporation of the drop, while the upper limit minimizes additional stretching of the film as the size of deformations of the film increased during measurements.

The temperature of the system was increased in 5 °C increments up to 95 °C at a rate of 90 °C/min., remaining at each temperature for 5 minutes to allow the drops to reach an equilibrium contact angle before images were captured. For measurements above 95 °C, the temperature was increased to the desired temperature at the same rate, at which point images were captured at 15 second intervals. For measurements of bulge dynamics above T_g, samples were prepared in the same manner, using polyethylene glycol (PEG) with $M_w = 0.6$ kg/mol (Sigma-Aldrich) in place of glycerol to reduce the effects of evaporation at high temperatures.

The radius of the contact patch the drop makes with the substrate r_c shown in Figure 3.1 was measured directly from the microscope images, and the profiles were fit to spherical caps. Examples are shown in Figure 3.1 (B). From these fits, the radius of curvature of the drop and bulge R_d and R_b were determined. The contact angle subtended by the spherical caps and the undeformed film θ_d and θ_b could be determined through the geometric identitiy, $\sin(\theta) = R/r_c$.

3.4 Results and Discussion

3.4.1 Determining Tension

It has been shown previously that in the limit of thin, highly bendable films deformed by drops with radii $r >> L_{\mathrm{BC}} >> L_{\mathrm{EC}}$ where the deformation caueses a significant

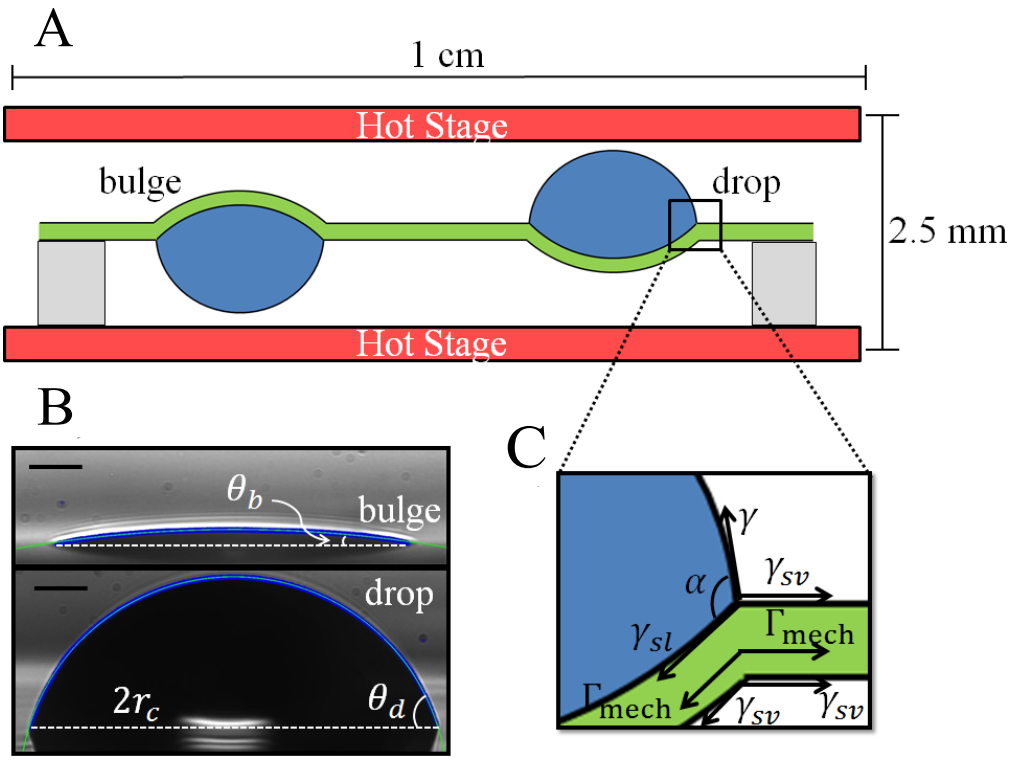

Figure 3.1: (A) Schematic of the side-view of glycerol drops on either side of a film between two temperature-controlled plates, not to scale. (B) Microscope image of a bulge (top) and drop (bottom) with spherical cap fits (blue curves). The contact diameters $2r_c$ are indicated with dashed lines. Below these lines is the reflection of the bulge/droplet off the film itself. The scale bar corresponds to 25 μm (C) Neumann construction accounting for interfacial and mechanical tension acting at the contact line of a drop. The interior angle α is the sum of θ_b and θ_d.

change in area of the film, anisotropic tensions are observed leading to striking wrinkling patterns around the liquid drop [31, 41]. However, if the deformation in the film is only a small perturbation to the area of the film, the tension in the film can be assumed isotropic and therefore can be determined by constructing a Neumann triangle at the contact line which includes both interfacial tensions and mechanical tension within the film due to elasticity [29]. Figure 3.1 (C) is a schematic of the tensions acting at the contact line. By balancing these tensions in the vertical direction, an expression relating θ_d and θ_b to the tension in the film can be found;

$$\frac{\sin(\theta_d)}{\sin(\theta_b)} = \frac{\Gamma_{\text{mech}} + \gamma_{sv} + \gamma_{sl}}{\gamma}, \tag{3.1}$$

where γ, γ_{sv} and γ_{sl} are the liquid-vapor, solid-vapor, and solid-liquid interfacial tensions, and Γ_{mech} is the mechnical tension within the film.

Equation 3.1 shows that by simultaneously measuring a drop and bulge contact angle for a particular film at a particular temperature, the tension in the film normalized by the surface tension of glycerol can be determined provided a drops are smaller than L_{GC} and the deformation in the film is a perturbation to the area of the film. The latter requirement is achieved by preparing samples with clamped boundaries and a significant mechanical pre-tension. The accuracy of this technique has been confirmed elsewhere by comparison with micropipette deflection techniques [29]. By measuring the tension in films of various thicknesses at different temperatures, the way the contact angles of drops and bulges on deformable free-standing films are affected by the tensions in the film can be found.

The normalized tension within the film is shown as a function of temperature for various film thicknesses in Figure 3.3. As seen in the plot, the normalized tension

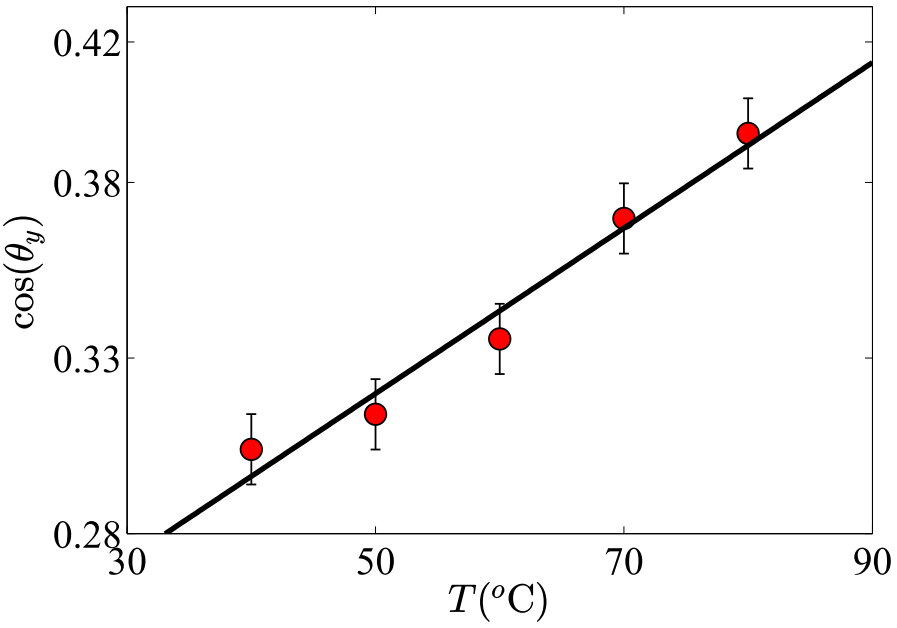

Figure 3.2: Contact angle of glycerol drops on a thin, supported PS substrate as a function of temperature.

decreases with temperature as well as film thickness. Young's angle θ_y for glycerol and PS as a function of temperature can be measured and is shown in Figure 3.2. The data in Figure 3.2 is well described by a linear relationship of the form $\cos(\theta_y) = aT+b$ where $a = (0.24 \pm 0.08) \cdot 10^{-2}$ °C^{-1} and $b = (20 \pm 5) \cdot 10^{-2}$. Using this empirical relationship along with literature values for γ of glycerol [42] and γ_{sv} of PS [43], γ_{sl} as a function of temperature is calculated. Finally, subtracting $(\gamma_{sv} + \gamma_{sl})/\gamma$ from the normalized tension given in Equation 1 yields $\Gamma_{\text{mech}}/\gamma$ as a function of temperature and film thickness.

Changes in mechanical tension upon heating are predominantly caused by the thermal expansion of the PS films which is much larger than rather than the thermal expansion of the steel. The film is fixed to the steel washer, so ignoring the contraction

of the steel washer, a decrease in temperature of the system results in a uniform strain ΔL within the film given by $\Delta L = c_{PS}\Delta T/(1-\nu)$ where $c_{PS} = 7 \cdot 10^{-6}$m/(m K) is the linear expansion coefficient of PS and $\nu = 0.34$ is the Poisson ratio of PS [44]. For an elastic membrane, the mechanical tension is equal to $\Gamma_{\text{mech}} = \sigma h = hE\Delta L/(1-\nu)$, where σ is the uniform stress within the film. Normalizing $\Gamma_{\text{mech}}/\gamma$ by film thickness should thus collapse our data to a single line, as seen in Figure 3.3 We fit a straight line to the data below 97 °C, while constraining it to pass through the point $\Gamma_{\text{mech}}/\gamma h = 0$ at $T = T_g = 97$ °C, which is the glass transition of PS [44]. Above T_g the film is a liquid which cannot have a mechanical tension. The constraint on the line of fit reflects this quality of PS. Using values for c_{PS} and ν from literature and the slope of this line, E for the PS films are found to be 3.0 ± 0.4 GPa which agrees with literature values [44]. The linear expansion coefficient of steel is dependent on its alloy composition so an exact value could not be found, however the expansion coefficients of several common stainless steel alloys are approximately $1/10^{\text{th}}$ that of PS [45]. Therefore the lower bound on E is expected to be approximately 10% lower than the true value.

3.4.2 Contact Angle and Tension

Considering the Neumann construction in Figure 3.1 (C), the tensions acting in parallel directions at the contact line can be grouped together (inwards; $\Gamma_{\text{in}} = \gamma_{sl} + \Gamma_{\text{mech}} + \gamma_{sv}$, in the plane of the film; $\Gamma_{\text{out}} = \Gamma_{\text{mech}} + 2\gamma_{sv}$) [29]. Using the cosine law can be used to calculate both θ_d and θ_b resulting in:

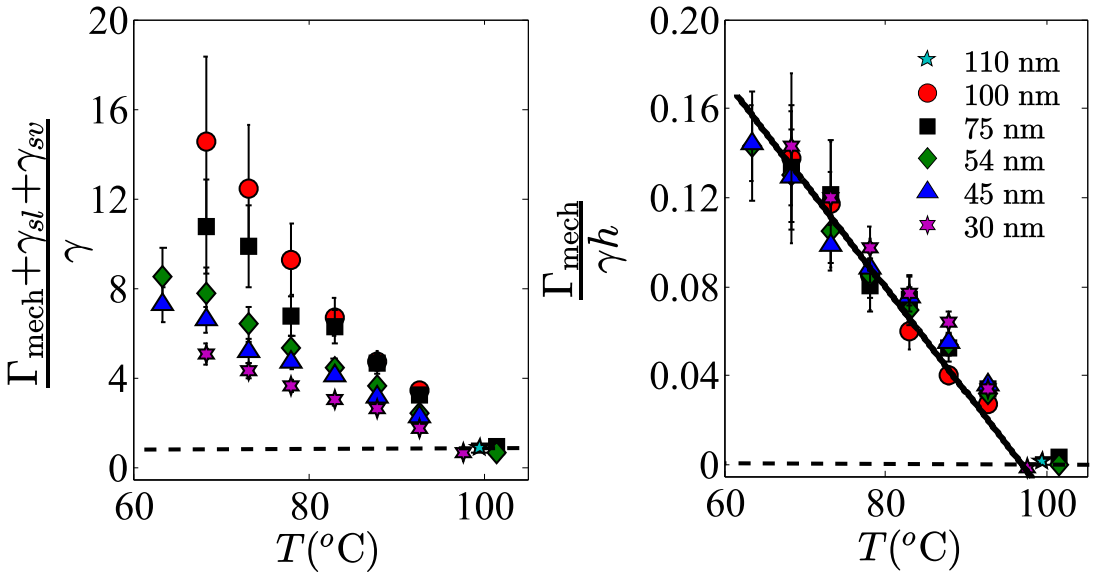

Figure 3.3: Tension within the PS film normalized by γ as a function of temperature for several film thicknesses is shown on the left. Mechanical tension within the film normalized by γ and h is shown on the right. A straight line with an x-intercept of 97 °C is fit to the data.

$$\cos(\theta_d) = \frac{(\Gamma_{\text{out}}/\gamma)^2 + 1 - (\Gamma_{\text{in}}\gamma)^2}{2\Gamma_{\text{out}}/\gamma} \tag{3.2a}$$

$$\cos(\theta_b) = \frac{(\Gamma_{\text{out}}/\gamma)^2 - 1 + (\Gamma_{\text{in}}\gamma)^2}{2\Gamma_{\text{out}}\Gamma_{\text{in}}/\gamma}. \tag{3.2b}$$

Recognizing $\Gamma_{\text{out}} = \Gamma_{\text{in}} + \gamma\sin(\theta_y)$, Equation 2 allows for the prediction of θ_d and θ_b as a function of $\Gamma_{\text{in}}/\gamma$, only requiring that θ_y be measured separately. Figure 3.4 shows θ_d and θ_b as a function of $\Gamma_{\text{in}}/\gamma$ for one film thickness. However, the experiment described here uses temperature as well as film thickness to modulate Γ_{in}, so θ_y will also change within a single experiment. Over the range of temperatures in this experiment, $\cos(\theta_y)$ is well described as a linear function of temperature. Likewise, Figure 3.3 shows the temperature dependence of Γ_{in}/γ can be approximated by a straight line until T_g is reached. Therefore, θ_y is expected to take on the functional form $\theta_y(\Gamma_{\text{in}}/\gamma) \propto \cos^{-1}(\Gamma_{\text{in}}/\gamma a\ + b - 97°\text{C})$ between 60 and 97 °C. Finally, Γ_{in} was calculated for a 54 nm film at 60 °C and 101.5 °C using the linear fit from Figure 3.3, temperature data could be converted to Γ_{in}, allowing for the prediction of θ_d and θ_b as a function of Γ_{in} while varying temperature. This prediction is show in Figure 3.4 represented by a solid line.

3.4.3 Dynamics

With this model, the growth of θ_b above T_g is believed to be through viscous relaxation. PEG drops were placed on 100 ± 5 nm free-standing PS films at 95 °C for 5 minutes to allow the system to reach an equilibrium contact angle. The temperature was increased to a final temperature (98 °C, 100 °C, or 101.5 °C) and measured until

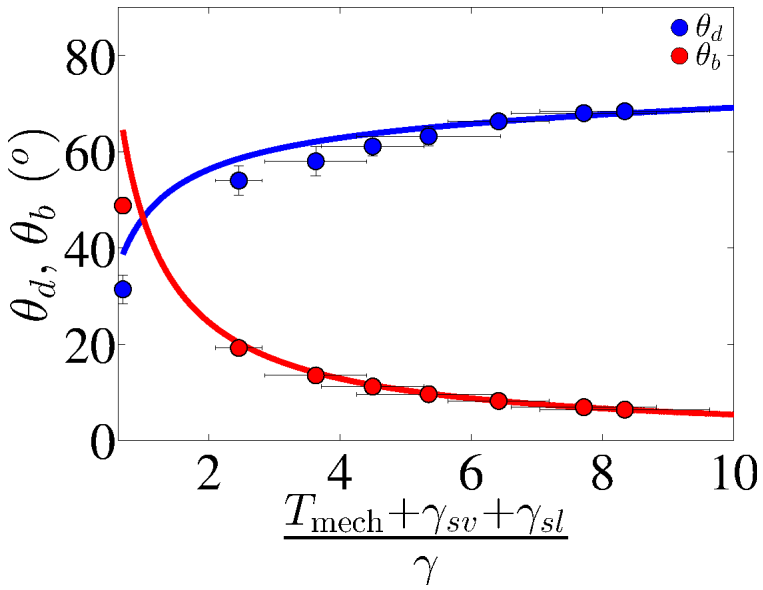

Figure 3.4: θ_d (blue circles) and θ_b (red diamonds) as a function of film tension normalized by γ for a 54 nm film. Contact angles predicted by a Neumann triangle at the contact line for a 54 nm film where tension is modulated by temperature is shown as solid lines, while the upper and lower dashed lines are at fixed temperatures (60 °C and 101.5 °C respectively), which correspond to the range of temperatures used in this particular data set.

film rupture, imaging the bulge in 15 second increments. The contact angles were normalized by the contact angle measured at 95 °C, θ_i, and the equilibrium contact angle measured at this elevated temperature θ_{eq}. The results are shown as a function of time in the inset of Figure 3.5. The average of up to the first four data points which were all within 1 °C of each other were used to determine θ_{eq} for each sample, and were found to be 19.1°, 18.9° and 21.1° for 98 °C, 100 °C, or 101.5 °C respectively. The contact angle predicted by a Neumann construction was found to be $\sim 24°$.

When the temperature of the system is raised suddenly, the temperature of the film and drops should increase almost instantaneously due to their small thermal masses. Likewise, interfacial tensions to also increase quickly. This creates an imbalance between Laplace pressure in the drop and pressure due to tension in the film which is what drives the growth of θ_b. Below T_g the rate of growth should be related to the rate of thermal expansion in the film. Above T_g, the film is in a melt state which cannot support a mechanical tension. Therefore the growth of θ_b should be related to the viscous relaxation of PS. Re-scaling the time over which θ_b changes by the ratio of viscosities of PS at 100 °C and the viscosity of PS at the measured temperature (calculated with the Vogel-Fulcher-Tammann equation [44]) causes the data to collapses to one curve suggesting that viscosity determines the rate of relaxation of our film above T_g.

If the temperature of the system is increased too quickly, a transient, negative mechanical tension can develop in the film due to thermal expansion which in some cases can manifest as buckles in the film. The increase in curvature in the film would be energetically unfavorable, and these buckles would undergo viscous relaxation. For temperatures used in these experiments, no obvious buckles were observed, however

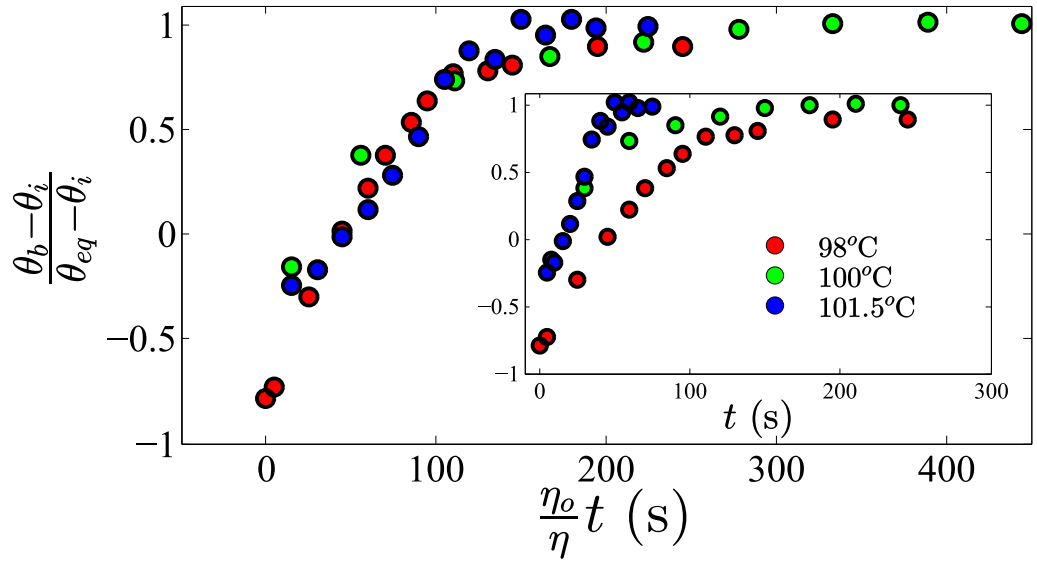

Figure 3.5: The bulge contact angle normalized by θ_i and θ_{eq} as a function of time normalized by the ratio of the viscosity of PS at the temperature measured and the calculated viscosity of PS at 100 °C. The inset shows the same data as a function of unscaled time.

Figure 3.5 shows a small rightwards shift in the data at 101.5 °C. It is possible that this is due to a small amount of buckling in the film.

3.5 Conclusions

In this work, thin glassy films were deformed by the Laplace pressure of sessile liquid drops. The contact angles made by the droplets and corresponding deformations with the underformed film were measured as tension was continuously varied by tuning film thickness and temperature. Through a Neumann construction at the contact line, it was found that the contact angle of the drop and bulges could be predicted as a function of temperature and film thickness. From this data the Young's modulus of PS was deduced. Furthermore, it is shown that as the film is raised above the glass transition, the mechanical stress in the film vanishes at which point it enters the regime of partial wetting of a liquid on a liquid substrate.

Bae et al. presented a method for determining elastic modulus of thin polymer films with liquid drops [12]. Nadermann et al. used a similar experiment to measure solid interfacial tensions [27]. Likewise, we have shown that droplets atop glassy, free-standing films are well described by a force balance at the contact line incorporating three interfacial tensions and a mechanical tension. Knowing any three of these variables allows for the determination of the fourth with reasonable accuracy.

Chapter 4

Fibers and Bubbles

4.1 Preamble

The following chapter contains significant portions of a manuscript intended for a peer-reviewed publication. It is closely related to a manuscript currently submitted for publication in which I made theoretical and experimental contributions [46]. In that work, a fiber is observed to bend more as the size of the contacting droplet is increased. At a critical droplet size, proportional to the bending elastocapillary length, the fiber is seen to spontaneously wind around the droplet. In this work a novel process for the self-assembly of fiber coils is presented. A model based on elastic beam theory is developed and found to accurately describe experimental data, resulting in an accurate prediction for the onset of this self-assembly process. We believe this process can be used to produce micro-coils of various materials.

In the manuscript presented below, a fiber is brought into contact with an air bubble emerging from a liquid bath. As the membrane of liquid forming the bubble wall thins, the contacting fiber is able to bridge the membrane. For certain combinations

of bubble size and fiber diameter, the fiber is found to spontaneously wrap around the circumference of the bubble. A theory based on interfacial and bending energies is presented which accurately predicts the onset of winding. I developed the theory and wrote the manuscript presented below in consultation with Schulman and Dalnoki-Veress. I performed the experiments with significant help from K. Charlesworth, an undergraduate research assistant.

4.2 Introduction

Wetting of planar surfaces are attractive systems to study due to their simple geometry, however liquids which wet fiberous materials are also interesting on both a fundamental and practical level. Despite seeming like a simple class of problems, liquid drops partially wetting fibers can be complicated. Even the case of a liquid drop partially wetting an undeformable, rigid rod can be complex as it may take on one of two equilibrium states: an axisymmetric "barrel" where the fiber penetrates the drop, and non-axisymmetric "clam-shell" configurations where the fiber arcs around the circumference [6, 7, 47–49]. In a series of beautiful experiments it was shown that drops placed on a taut elastic fiber would reach a barrel configuration [50, 51]. With reduced tension, these fibers would buckle and collapse inside the drop if the radius of the drop was on the order of L_{BC} or greater. As the fiber coils inside the drop, a consistent tension in the fiber is maintained – much like a windlass. This incredible process is in fact used by some types of spiders in web construction [51]. Alternatively, for smaller drop to fiber radius ratios or less wettable combinations of materials, the clam-shell configuration may be observed [9, 49]. In this case capillary forces are capable of inducing large deformations in the fiber resulting in the fiber

wrapping *around* the drop, which is the subject of the work by Schulman et al. which I made contributions to [46]. In both cases, length-scale of these deformations can be determined by balancing elastic bending and capillarity, resulting in the bending elasto-capillary length, $L_{\mathrm{BC}} = \sqrt{Er^3/\gamma}$ where E is the elastic modulus, r is the fiber radius, and γ is the liquid-air surface tension. Large-scale deformations in the fiber are expected when capillary forces act over lengths greater than L_{BC}.

In this chapter, air bubbles below the surface of a liquid bath are used to deform the surface of the bath into an approximately spherical cap defined by a thin liquid membrane. This is shown schematically side-on in Figure 4.1 (A). Microfibers are placed on top of the deformed surface. The fiber is found to migrate to and wrap around the perimeter of the deformed liquid surface for certain bubble-fiber radius ratios. Optical images of this process, viewing the top of the air bubble, are shown in Figure 4.1 (B) and (C). This process is characterized by balancing the interfacial and bending energies of the system.

4.3 Experiment

Thin polymer fibers were made from several materials: Polystyrene (PS) with molecular weight $M_n = 25000$ kg/mol and polydispersity PDI = 1.04 (Polymer Source Inc.) which is a glass at room temperature, Elastollan 1185A 10 (BASF Inc.) which is a polyether-based physically cross-linked elastomer which is solid at room temperature, and styrene-isoprene-styrene (SIS) triblock copolymer (14% styrene content, Sigma-Aldrich), which is a physically crosslinked elastomer at room temperature. PS and Elastollan fibers were made using a glass micropipette with an inner diameter of 0.7 mm and outer diameter of 1.0 mm (World Precision Instruments Inc.), pulled and

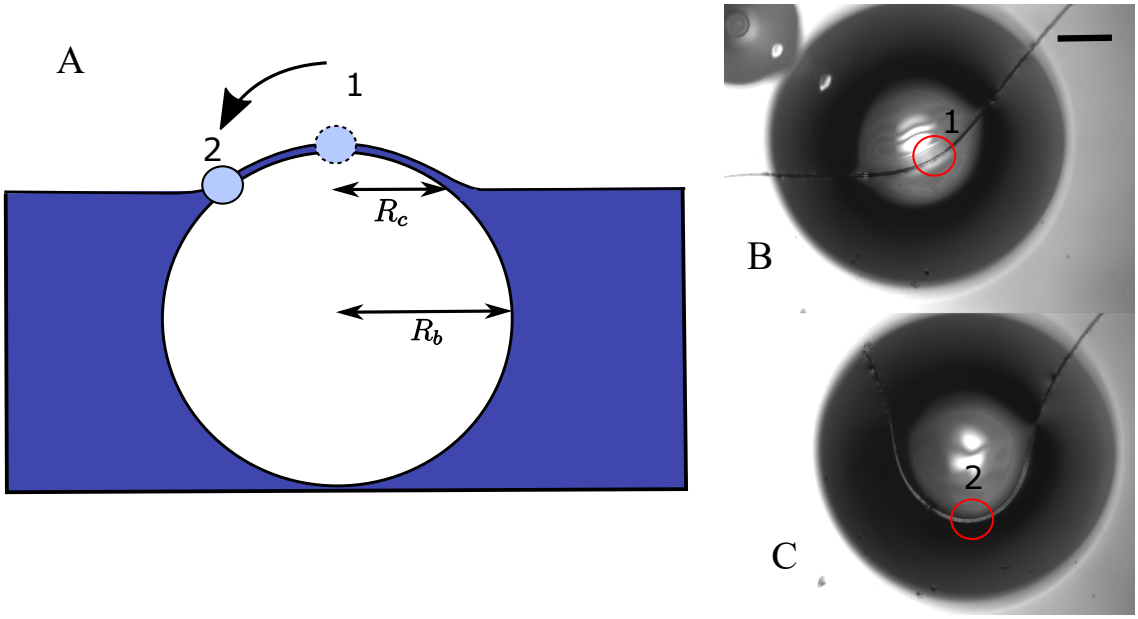

Figure 4.1: (A) Schematic of the fiber-bubble system side-on. The fiber is shown in light blue in position 1 and 2, representing the pre-flopped and post-flopped positions of the fiber. (B) and (C) are top-down optical images of a fiber-bubble system before and after flopping. Red circles indicate the point of the fiber that the schematic cross-section represents. The scale bar is 250 μm.

clipped to have a short tapered end with an inner diameter of ~ 10 μm and an outer diameter of ~ 20 μm as described in Chapter 2. The tapered end was dipped into the polymer – which was held at 170 °C for PS and 235 °C for Elastollan – and then quickly pulling the pipette out. The resulting fibers had radii between $1\ \mu\text{m} < r < 10\ \mu\text{m}$, as measured by optical microscopy. Fibers of similar dimensions were made from SIS by dipping a micropipette into a viscous solution of the polymer dissolved in toluene and quickly pulling the pipette out.

Once a fiber was made it was placed atop a glycerol bath. Small air bubbles were blown below the surface of the bath, directly below the fiber, with a micropipette with the same dimensions as the micropipette described above, connected to a syringe filled with air. As the bubble rises due to buoyancy, the surface of the film as well as the fiber are pushed above the undeformed surface of the bath into a cap-like shape. A side-on schematic of this process as well as two optical images of the process are shown in Figure 4.1. This cap has some curvature which causes glycerol to drain from the curved surface into the undeformed bath, resulting in the thinning of the deformed glycerol layer. The thinning process is observed optically by imaging the cap with monochromatic light. Depending on the film thickness, the light will constructively or destructively interfere with itself as it passes through the film and is reflected back to the objective. The film begins with a uniform color and with time, interference fringes form. An example of these fringes is shown in Figure 4.2. The fringes move radially outward, signifying that material is moving from the centre, outwards.

When the cap reaches a critical thickness, the fiber will bridge across the liquid membrane as shown schematically in Figure 4.3. At this point, the fiber may begin to migrate down the cap toward the circumference of the light circle which demarcates

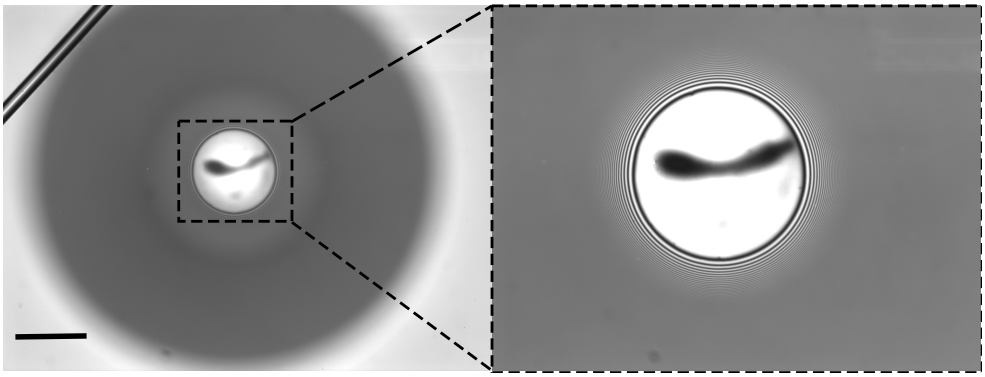

Figure 4.2: Optical image of an air bubble rising from below the surface of a glycerol bath, taken with monochromatic light. This scale bar is 250 μm. As the air bubble rises, the surface of the bath becomes deformed into an approximately spherical cap creating a thin glycerol membrane above the undeformed surface of the bath. As the membrane thins, interference fringes (black and white concentric circles) form and move radially outward. As the bubble reaches its equilibrium height above the surface of the bath, a single distinct inner circle emerges like in Figure 4.1.

where the cap converges with the undeformed surface of the bath. This process is shown in Figure 4.1. The outer radius of the bubble R_b and inner radius R_c – which is located at the circumference of the light circle – are measured optically. If the fiber migrates all the way to the inner circumference, it is considered to have "flopped". In some instances where the fiber is thin and readily deformed and the air bubble is large, this migrating process can be replaced by the fiber creating an S-like shape on the cap as a large extent of fiber is pulled on to the cap. An example of this is shown in Figure 4.4 (A). The experiments are limited to fiber-bubble size combinations where this will not happen.

After the fiber has migrated to the edge of R_c, the fiber may continue to wrap around the circumference of R_c similar to Figure 4.4. This appears to continue until the fiber is unable to continue bridging the increasingly thick glycerol membrane, an

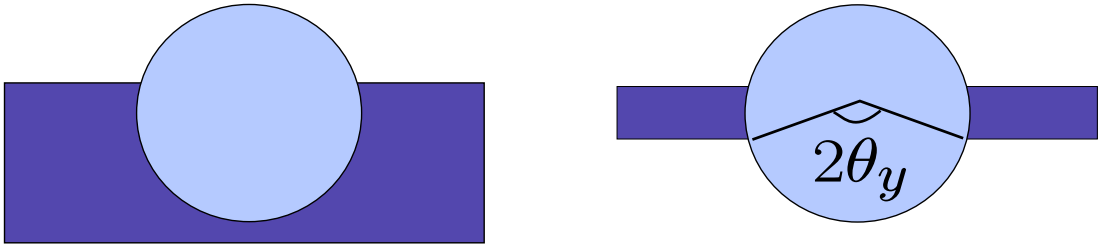

Figure 4.3: Schematic of an end-on fiber sitting atop a fluid bath and an end-on fiber bridging a fluid film.

imperfection in the fiber or bath (such as a dust particle) slows its progression, or the bubble pops, however, this process is not yet fully understood. Bubbles for which a fiber has stopped winding but have not immediately popped have been observed to last for several hours

4.4 Results and Discussion

In the experiment described above, an air bubble is produced below the surface of a glycerol bath which deforms the surface of the bath creating a "cap" that extends above the surface of the glycerol as shown in Figure 4.1. A thin polymer fiber (Elastollan, SIS or PS) is laid across the cap and as the glycerol film forming the cap thins, the fiber "bridges" across the film and in some instances, will "flop" to one side of the cap. Figure 4.3 schematically shows an end-on cross-section of the fiber in the unbridged and bridged orientations. The bridging process removes a solid-liquid and liquid-vapor interface and replaces it with an solid-vapor interface. Bridging results in a change in interfacial energy per unit length,

$$\frac{\Delta E_{\text{surf}}}{L} = (2r\theta_y(\gamma_{sv} - \gamma_{sl}) - 2r\gamma\sin(\theta_y)) \tag{4.1}$$

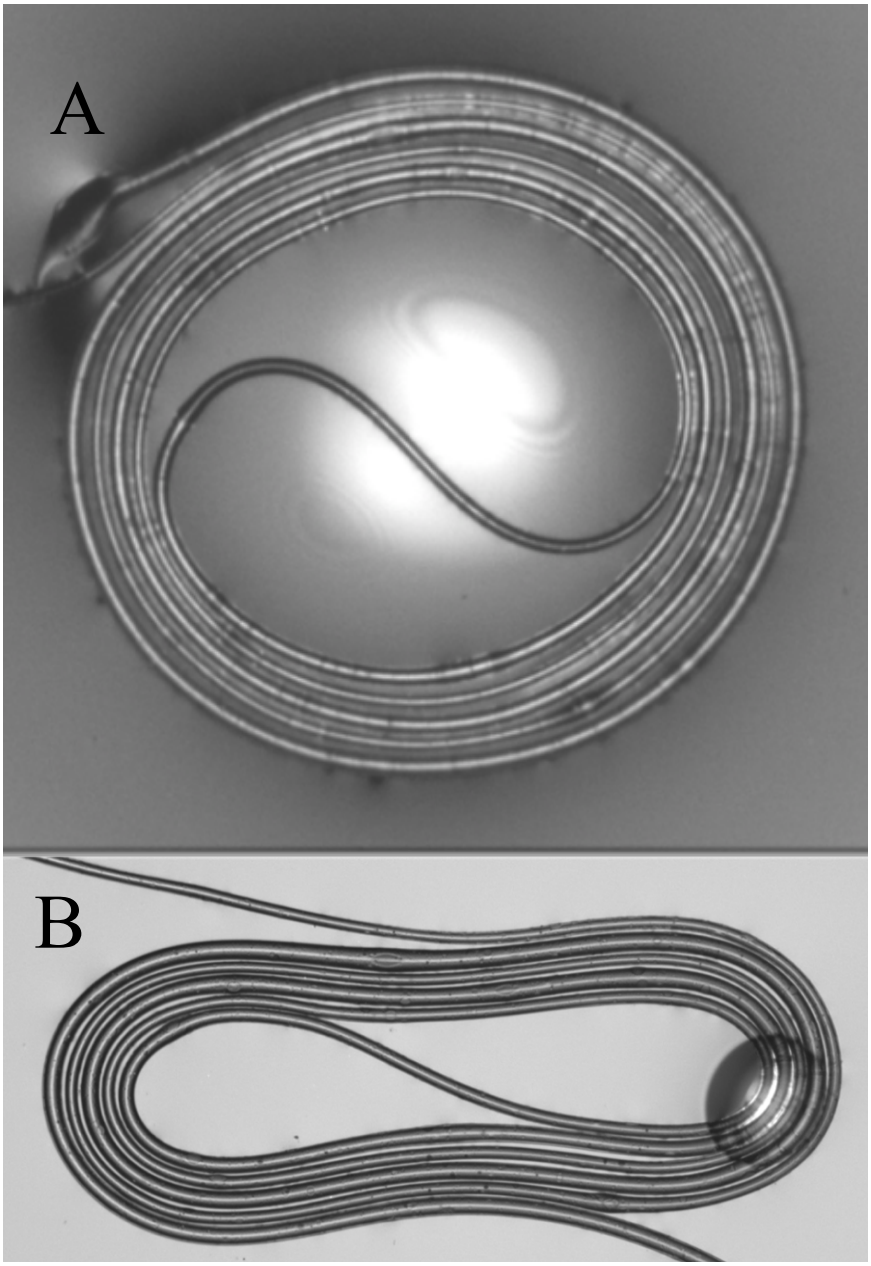

Figure 4.4: (A SIS fiber of $r \approx 5$ μm winds around an air bubble on a glycerol bath before (A) and after (B) the bubble pops.

where L is the length of fiber which bridges, r is the radius of the fiber, θ_y is the Young's angle made between glycerol and fiber material, γ_{sv} is the solid-vapor interfacial tension, and γ_{sl} is the solid-liquid interfacial tension. When this parameter is negative, it is more favorable for the fiber to be in the bridged state. This creates a tendency for the fiber to be pulled on to the bubble and subsequently wind around the perimeter of the cap – the longer the length of fiber that bridges, the larger the reduction in interfacial energy in the system.

Initially, the fiber is laid across the top surface of the air bubble. As more fiber is pulled on to the air bubble, the fiber must reorient to accommodate this extra length. The easiest way to achieve this is for the fiber to "flop" to one side of the air bubble. Figure 4.1 shows a top-view of a fiber-bubble system before and after a flopping event. This type of flopping event allows for an increase in the length of fiber which bridges, while minimizing bending energy - a term which will be described later. Higher order bending may occur involving multiple inflection points, but these events are less likely due to the higher bending energy associated with these shapes.

Calculating the change in interfacial energy of the system during a flopping event is done by applying Equation 4.1 to the change in length of fiber which is bridged in Figure 4.1 (A) and (B). To determine this lenght a description of the shape of the glycerol-air cap is required. For small bubbles it has been shown that the Laplace pressure of the bubble is high enough that gravity does not significantly alter its shape, such that the entire air bubble can be treated as being spherical [52]. Outside R_c the thickness of the glycerol film thickens which makes it impossible for the fiber to bridge beyond the point where the thickness is greater than the radius of the fiber. Qualitatively, it is found that a fiber that flops to the side of an air bubble will stop

at R_c, taking on a radius of curvature given by R_c. By measuring R_b and R_c optically, we can measure the curvature in the fiber in both the flopped (R_c) and unflopped ($R_b \sin^{-1}(R_c/R_b)$ positions. Using this information we can calculate the total change in interfacial energy,

$$\Delta E_{\text{surf}} = (2r\theta_y(\gamma_{sv} - \gamma_{sl}) - 2r\gamma\sin(\theta_y)) \left(\pi R_c - 2R_b \sin^{-1}\left(\frac{R_c}{R_b}\right)\right), \tag{4.2}$$

where the $2\sin^{-1}(\frac{R_c}{R_b})$ term is equal to the angle defining the arc length of the cap shown in the cross-sectional schematic of Figure 4.1 (C) which is geometrically similar to Figure 4.3. Using Young's law, $\gamma\cos(\theta_y) = \gamma_{sv} - \gamma_{sl}$, Equation 4.2 becomes,

$$\Delta E_{\text{surf}} = (2r\gamma(\theta_y\cos(\theta_y) - \sin(\theta_y))) \left(\pi R_c - 2R_b \sin^{-1}\left(\frac{R_c}{R_b}\right)\right). \tag{4.3}$$

Equation 4.3 accounts for the difference in energy between a fiber floating on a bath and bridging a film, and is applied across the difference in length between the fiber lying atop the cap and wrapping exactly half-way around the perimeter of the cap. We find qualitatively that the fiber will bridge across the diameter of a bubble and the points of the fiber on the circumference of the bubble remain roughly fixed which, if a fiber flops, will result in a fiber which wraps half-way around the bubble.

Since this new radius is smaller than the maximum radius of the air bubble, there is an increase in bending energy associated with "flopping" to one side of the air bubble which is given by,

$$\Delta E_{\text{bend}} = \frac{\pi E r^4}{8}\left(\frac{\pi R_c}{R_c^2} - \frac{2R_b\sin^{-1}(\frac{R_c}{R_b})}{R_b^2}\right), \tag{4.4}$$

where E is the elastic modulus of the fiber. Accounting for both the difference in

interfacial energy and bending energy before and after flopping ($\Delta E_{\text{total}} = \Delta E_{\text{surf}} + \Delta E_{\text{bend}}$), a value of $\Delta E_{\text{total}} < 0$ would result in spontaneous flopping. We can define a "flopping" criteria by setting the change in energy equal to zero,

$$\begin{aligned}\Delta E_{\text{total}} &= 0 \\ &= (2r\gamma(\theta_y \cos(\theta_y) - \sin(\theta_y)))\left(\pi R_c - 2R_b \sin^{-1}\left(\frac{R_c}{R_b}\right)\right) + \\ &\frac{\pi E r^4}{8}\left(\frac{\pi R_c}{R_c^2} - \frac{2R_b sin^{-1}(\frac{R_c}{R_b})}{R_b^2}\right).\end{aligned} \tag{4.5}$$

Equation 4.5 can be re-arranged to define a function $F(R_c, R_b) = \frac{\pi R_c^2 - 2R_c R_b sin^{-1}(\frac{R_c}{R_b})}{\pi - 2sin^{-1}(\frac{R_c}{R_b})\frac{R_c}{R_b}}$ which depends exclusively on E, r, θ_y, and γ:

$$\frac{\pi R_c^2 - 2R_c R_b \sin^{-1}\left(\frac{R_c}{R_b}\right)}{\pi - 2\sin^{-1}\left(\frac{R_c}{R_b}\right)\frac{R_c}{R_b}} = \frac{\pi E r^3}{16(\sin(\theta_y) - \theta_y \cos(\theta_y))\gamma}. \tag{4.6}$$

E, θ_y, and γ can be measured independently, and using fibers and bubbles of various sizes, $F(R_c, R_b)$ can be calculated. $F(R_c, R_b)$ is plotted as a function of $\frac{Er^3}{(sin(\theta_y) - \theta_y cos(\theta_y))\gamma}$ in Figure 4.5 for various fiber materials. A fiber that migrates to the perimeter of the cap is considered a successful flop, and the point is plotted in green. Otherwise, if the fiber does not reach the perimeter of the cap, the point is plotted in red. By plotting $\frac{Er^3}{sin(\theta_y) - \theta_y cos(\theta_y)\gamma}$ on the x-axis, the theory predicts a slope of $\frac{\pi}{16}$, independent of fiber and fluid material. This line is shown to in Figure 4.5 in excellent agreement with the data.

After flopping, the bridging phenomenon still drives the movement of fiber from the bath to the bubble. Likewise, this creates an increase in the curvature of the fiber

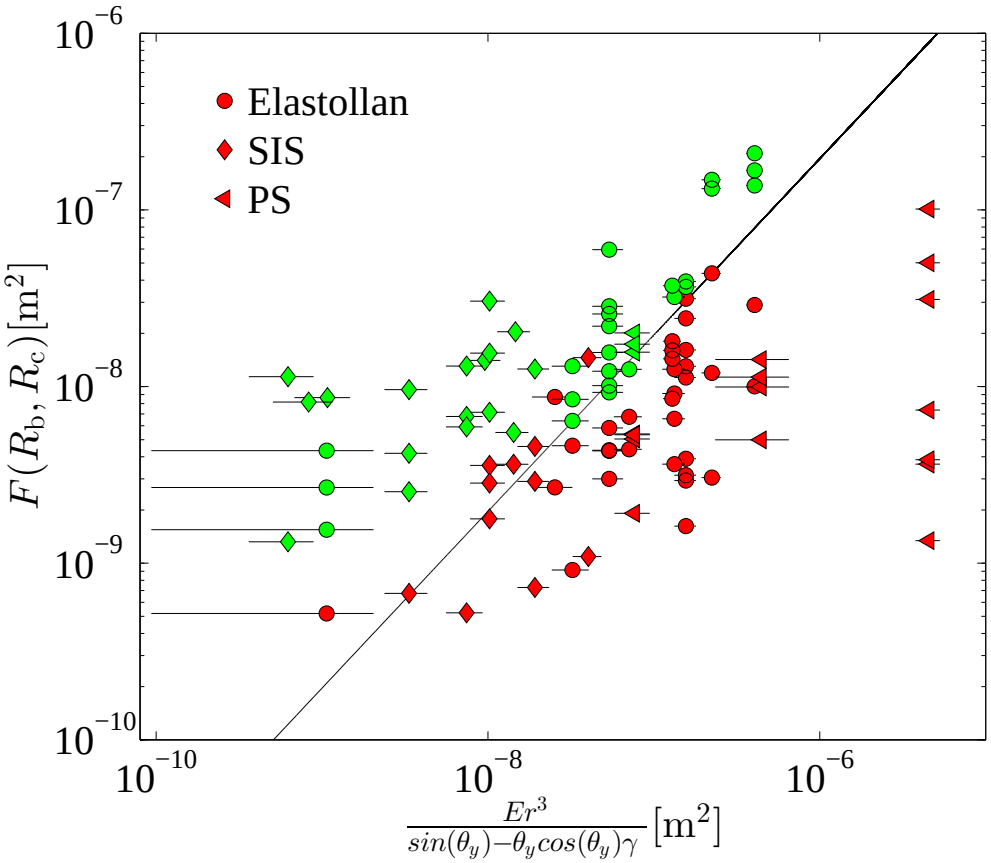

Figure 4.5: Phase diagram of the flopping transition for Elastollan (circles), SIS (diamonds) and PS (triangles) fibers in glycerol. $F(R_c, R_d)$ is a function related to the geometric properties of the air bubble. The slope defining the transition is $\frac{\pi^2}{16}$.

as the fiber takes on a radius of curvature R_c. Balancing these changes in energy as was done previously, a winding threshold can be calculated,

$$R_c^2 = \frac{\pi E r^3}{16(sin(\theta_y) - \theta_y cos(\theta_y))\gamma}. \tag{4.7}$$

For bubbles above this threshold (or conversely, fibers below a certain thickness), the fiber will spontaneously wind around the bubble. This process is show in Figure 4.6.

Comparing Equation 4.6 and Equation 4.7, we find that the winding process will occur for a thicker fiber than the flopping process for a given bubble size. This means if a fiber flops, it will continue to wind around the bubble. Figure 4.4 (A) shows a SIS fiber that has wound many times around a bubble. SIS adheres to itself, so when the bubble Figure 4.4 (A) pops, a stunning fiber coil is left behind, shown in Figure 4.4 (B). We believe the non-circular shape of the fiber loop in Figure 4.4 (B) is due to a 3-dimensional, circular coil (recall the fiber is winding around a spherical cap) being confined to a 2-dimensional surface via surface tension.

4.5 Conclusions

In this work, a unique self-assembly process is presented which occurs when thin polymer fibers were brought in contact with air bubbles below the surface of a glycerol bath. The fibers were found to deform around the bubbles to allow longer lengths of fiber to bridge across the glycerol membrane, thus reducing the interfacial energy of the system. The decrease in interfacial energy of the fiber comes at a cost of increasing the bending energy of the system. A critical bubble size as a function

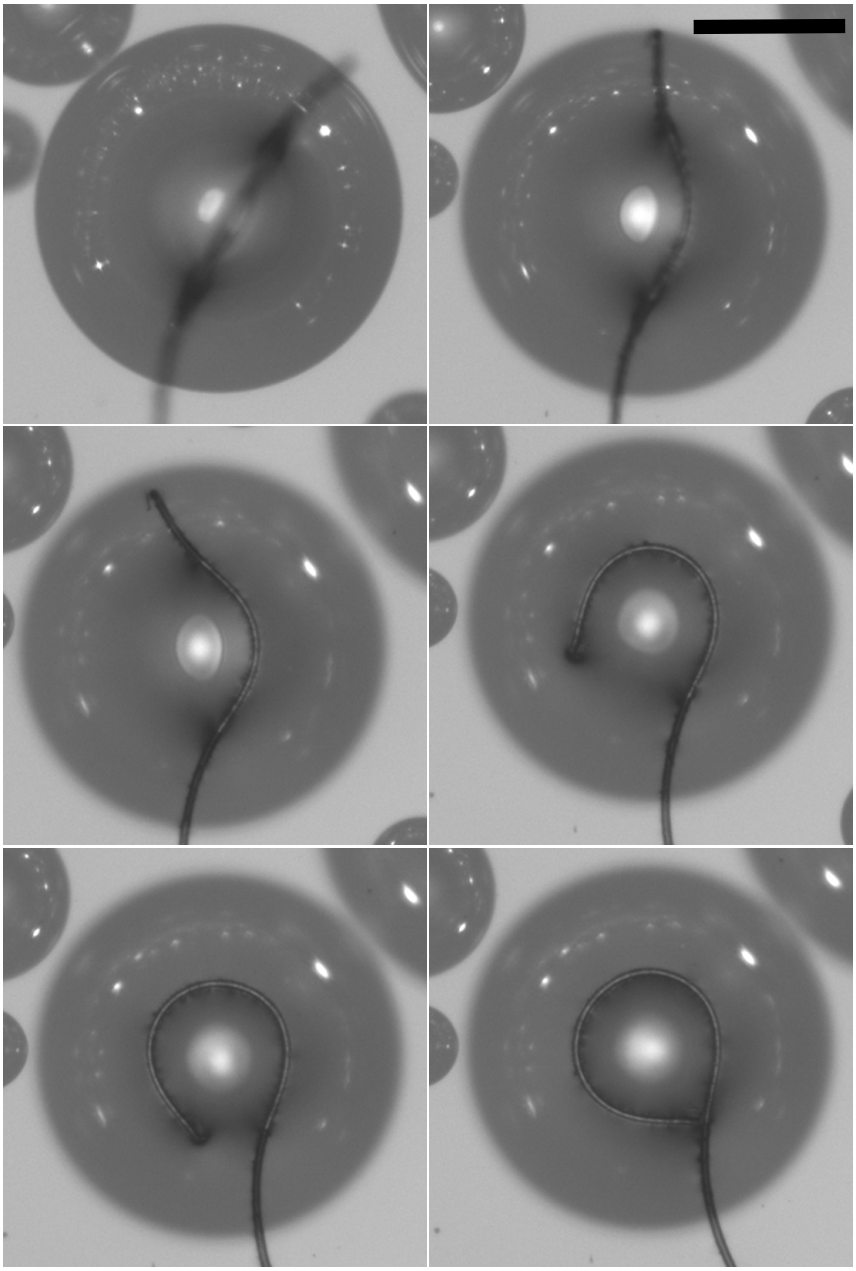

Figure 4.6: Spontaneous winding of a SIS fiber around an air bubble in a bath of glycerol. The scale bar in the top right frame is 200 μm.

of fiber material was derived for which fibers would spontaneously wind around a bubble, and was confirmed experimentally for several fiber materials.

Using solids to stabilize liquid bubbles is an active area of research [53–57]. Wrapping a bubble cap with a bridged fiber should be able to reduce the flow of material from high curvature back into the bath. The thinning of the liquid membrane is what ultimately causing bubbles to pop. It is found qualitatively that wound bubbles last longer than non-wound bubbles. In fact, some wound bubbles were observed to last for more than 12 hours. It is possible a deformable collection of fibers which spontaneously wrap around bubbles could be used as a bubble stabilizing technique. Additionally, it is possible that sufficiently thick or high-modulus fibers could be used in such an environment to arrange bubbles in a predetermined pattern. Finally, this is a method which can be used to spontaneously produce micron-sized circular polymer loops and coils.

Chapter 5

Conclusions

Elasto-capillarity is the ability of capillary forces to deform elastic structures. This phenomenon is found at all length scales in the natural world as well as industrial applications. However ubiquitous these effects may be, many fundamental questions still remain. In this thesis I have presented two main projects which elucidated elasto-capillary phenomena in the context of films and liquid drops, as well as fibers and bubbles.

In Chapter 3, the shape of elastic deformations in compliant polymer films as a function of tension in the film due to capillary forces from liquid drops was studied. By balancing interfacial and elastic tensions at the contact line, the interior angle of a liquid drop in contact with an elastic film was predicted as the tension in the film was modulated via temperature. While this chapter was limited to a simple system involving single drops on films of uniform tension, the interaction of several drops on both sides of a film has yet to be explored. Additionally, the use of non-symmetrically tensioned films may yield interesting and useful results.

In Chapter 4, the spontaneous winding of slender polymer rods around liquid

bubbles was investigated. A minimal interfacial energy model was developed and by balancing the free energy reduction predicted by this model with the increase in bending energy of the polymer rods, a winding criteria based on the dimensions and materials of the bubble and rod was found. The winding criteria was confirmed for several fiber materials. The winding phenomenon in isolation has yet to be fully understood, as well as the shape the 3-dimensional coil makes when confined to 2 dimensions. Additionally, the applications of this phenomena such as bubble stabilization and self-assembly of fiber loops have yet to be explored.

Bibliography

[1] J. Bico, B. Roman, L. Moulin, and A. Boudaoud. coalescence in wet hair. *J. Microelectromech. Syst*, 14, 2004.

[2] C. Py, P. Reverdy, L. Doppler, J. Bico, B. Roman, and C. N. Baroud. Capillary Origami: Spontaneous Wrapping of a Droplet with an Elastic Sheet. *Phys. Rev. Lett.*, 98(15), 2007.

[3] C. Duprat, S. Protire, A. Y. Beebe, and H. A. Stone. Wetting of flexible fibre arrays. *Nature*, 482(7386), February 2012.

[4] C. Duprat and S. Protiere. Capillary stretching of fibers. *Europhys. Lett.*, 111(5), 2015.

[5] A. Sauret, F. Boulogne, D. Cebron, E. Dressaire, and H. A. Stone. Wetting morphologies on an array of fibers of different radii. *Soft Matter*, 11, 2015.

[6] G McHale, N. A. Käb, M. I. Newton, and S. M. Rowan. Wetting of a High-Energy Fiber Surface. *J. Colloid Interface Sci.*, 186(2), 1997.

[7] B. J. Carroll. The equilibrium of liquid drops on smooth and rough circular cylinders. *J. Colloid Interface Sci.*, 97(1), 1984.

[8] D. Quéré. Fluid coating on a fiber. *Annual Review of Fluid Mechanics*, 31(1), 1999.

[9] B. Roman and J. Bico. Elasto-capillarity: deforming an elastic structure with a liquid droplet. *J. Phys-Condens. Mat.*, 22(49), 2010.

[10] N. Patra, B. Wang, and P. Krl. Nanodroplet Activated and Guided Folding of Graphene Nanostructures. *Nano Lett.*, 9(11), 2009.

[11] J. W. van Honschoten, J. W. Berenschot, T. Ondarcuhu, R. G. P. Sanders, J. Sundaram, M. Elwenspoek, and NR. Tas. Elastocapillary fabrication of three-dimensional microstructures. *Appl. Phys. Lett.*, 97(1), 2010.

[12] J. Bae, T. Ouchi, and R. C. Hayward. Measuring the Elastic Modulus of Thin Polymer Sheets by Elastocapillary Bending. *ACS Appl. Mater. Interfaces*, 7(27), 2015.

[13] O. Campás, T. Mammoto, S. Hasso, R. A. Sperling, D. O'Connell, A. G. Bischof, R. Maas, D. A. Weitz, L. Mahadevan, and D. E. Ingber. Quantifying cell-generated mechanical forces within living embryonic tissues. *Nat. Methods*, 11(2), 2014.

[14] J. B. Grotberg and O. E. Jensen. Biofluid mechanics in flexible tubes. *Annu. Rev. Fluid Mech.*, 36(1), January 2004.

[15] A. L. Hazel and M. Heil. Surface-tension-induced buckling of liquid-lined elastic tubes: a model for pulmonary airway closure. *P. R. Soc. A.*, 461(2058), June 2005.

[16] S. Shojaei-Zadeh, S. R. Swanson, and S. L. Anna. Highly uniform micro-cavity arrays in flexible elastomer film. *Soft Matter*, 5(4), 2009.

[17] R. W. Style, R. Boltyanskiy, Y. Che, J. S. Wettlaufer, L. A. Wilen, and E. R. Dufresne. Universal Deformation of Soft Substrates Near a Contact Line and the Direct Measurement of Solid Surface Stresses. *Phys. Rev. Lett.*, 110(6), 2013.

[18] A. Chakrabarti and M. K. Chaudhury. Direct Measurement of the Surface Tension of a Soft Elastic Hydrogel: Exploration of Elastocapillary Instability in Adhesion. *Langmuir*, 29(23), June 2013.

[19] P. G. de Gennes, F. Brochard-Wyart, and D. Quéré. *Capillarity and wetting phenomena: drops, bubbles, pearls, waves*. Springer, 2008.

[20] T. Young. An Essay on the cohesion of fluids. *Phil. Trans. R. Soc.*, 95, 1805.

[21] R. W. Style, Y. Che, S. J. Park, B. M. Weon, J. H. Je, C. Hyland, G. K. German, M. P. Power, L. A. Wilen, J. S. Wettlaufer, and E. R. Dufresne. Patterning droplets with durotaxis. *P. Natl. Acad. Sci. USA*, 110(31), July 2013.

[22] A. Marchand, S. Das, J. H. Snoeijer, and B. Andreotti. Contact Angles on a Soft Solid: From Youngs Law to Neumanns Law. *Phys. Rev. Lett.*, 109(23), December 2012.

[23] C. Y. Hui and A. Jagota. Deformation near a liquid contact line on an elastic substrate. *P. Roy. Soc. A-Math Phy.*, 470(2167), 2014.

[24] R. W. Style and E. R. Dufresne. Static wetting on deformable substrates, from liquids to soft solids. *Soft Matter*, 8(27), 2012.

[25] R. Pericet-Cámara, A. Best, H. J. Butt, and E. Bonaccurso. Effect of capillary pressure and surface tension on the deformation of elastic surfaces by sessile liquid microdrops: An experimental investigation. *Langmuir*, 24(19), 2008.

[26] E. R. Jerison, Y. Xu, L. A. Wilen, and E. R. Dufresne. Deformation of an Elastic Substrate by a Three-Phase Contact Line. *Phys. Rev. Lett.*, 106(18), May 2011.

[27] N. Nadermann, C. Y. Hui, and A. Jagota. Solid surface tension measured by a liquid drop under a solid film. *P. Natl. Acad. Sci. USA*, 110(26), 2013.

[28] C. Y. Hui, A. Jagota, N. Nadermann, and X. Xu. Deformation of a Solid Film with Surface Tension by a Liquid Drop. *Procedia IUTAM*, 12, 2015.

[29] R. D. Schulman and K. Dalnoki-Veress. Liquid Droplets on a Highly Deformable Membrane. *Phys. Rev. Lett.*, 115(20), 2015.

[30] S. J. Park, B. M. Weon, J. S. Lee, J. Lee, J. Kim, and J. H. Je. Visualization of asymmetric wetting ridges on soft solids with X-ray microscopy. *Nat. Commun.*, 5, 2014.

[31] J. Huang, M. Juszkiewicz, W. H. de Jeu, E. Cerda, T. Emrick, N. Menon, and T. P. Russell. Capillary Wrinkling of Floating Thin Polymer Films. *Science*, 317(5838), 2007.

[32] L. D. Landau and E. M. Lifshitz. *Theory of Elasticity*. Pergamon Press, 3rd edition, 2000.

[33] R. M. A. Azzam and N. M. Bashara. *Ellipsometry and Polarized Light*. North-Holland Publishing Company, Amsterdam, 1977.

[34] S. Karpitschka, S. Das, M. van Gorcum, H. Perrin, B. Andreotti, and J. H. Snoeijer. Droplets move over viscoelastic substrates by surfing a ridge. *Nat. Commun.*, 6, 2015.

[35] J. W. van Honschoten, J. W. Berenschot, T. Ondaruhu, R. G. P. Sanders, J. Sundaram, M. Elwenspoek, and N. R. Tas. Elastocapillary fabrication of three-dimensional microstructures. *Appl. Phys. Lett.*, 97(1), 2010.

[36] J. D. Paulsen, V. Démery, C. D. Santangelo, Thomas P. Russell, B. Davidovitch, and N. Menon. Optimal wrapping of liquid droplets with ultrathin sheets. *Nat. Mater.*, 14(12), 2015.

[37] S. Protiere, C. Duprat, and H. A. Stone. Wetting on two parallel fibers: drop to column transitions. *Soft Matter*, 9(1), 2013.

[38] H. Elettro, S. Neukirch, F. Vollrath, and A. Antkowiak. In-drop capillary spooling of spider capture thread inspires highly extensible fibres. *arXiv preprint arXiv:1501.00962*, 2015.

[39] A. Fargette, S. Neukirch, and A. Antkowiak. Elastocapillary Snapping: Capillarity Induces Snap-Through Instabilities in Small Elastic Beams. *Phys. Rev. Lett.*, 112(13), April 2014.

[40] G. R. Lester. Contact angles of liquids at deformable solid surfaces. *J. Colloid Interface Sci.*, 16, 1961.

[41] R. D. Schroll, M. Adda-Bedia, E. Cerda, J. Huang, N. Menon, T. P. Russell, K. B. Toga, D. Vella, and B. Davidovitch. Capillary Deformations of Bendable Films. *Physical Review Letters*, 111(1), July 2013.

[42] G. Korosi and E. S. Kovats. Density and surface tension of 83 organic liquids. *J. Chem. Eng. Data*, 26(3), 1981.

[43] S. Wu. Surface and interfacial tensions of polymer melts. II. Poly (methyl methacrylate), poly (n-butyl methacrylate), and polystyrene. *J. Phys. Chem.*, 74(3), 1970.

[44] J. Brandrup, E. H. Immergut, and E. A. Grulke. *Polymer Handbook*. Wiley, 4th edition, 1999.

[45] W. F. Gale and T. C. Totemeier. *Smithells metals reference book*. Butterworth-Heinemann, 2003.

[46] R. D. Schulman and K. Dalnoki-Veress. Liquid Droplets on a Highly Deformable Membrane. arXiv:1607.05990, 2016.

[47] B. J. Carroll. The accurate measurement of contact angle, phase contact areas, drop volume, and Laplace excess pressure in drop-on-fiber systems. *J. Colloid Interface Sci.*, 57(3), 1976.

[48] G. McHale and M. I. Newton. Global geometry and the equilibrium shapes of liquid drops on fibers. *Colloids Surf., A*, 206(1-3), 2002.

[49] T. H. Chou, S. J. Hong, Y. E. Liang, H. K. Tsao, and Y. J. Sheng. Equilibrium phase diagram of drop-on-fiber: Coexistent states and gravity effect. *Langmuir*, 27(7), 2011.

[50] H. Elettro, F. Vollrath, A. Antkowiak, and S. Neukirch. Coiling of an elastic beam inside a disk: A model for spider-capture silk. *Int. J. Nonlinear Mech.*, 75, 2015.

[51] H. Elettro, S. Neukirch, F. Vollrath, and A. Antkowiak. In-drop capillary spolling of spider capture thread inspires hybrid fibers with mixed solid-liquid mechanical properties. *PNAS*, 113(22), 2016.

[52] J. Hua and J. Lou. Numerical simulation of bubble rising in viscous liquid. *J. Comput. Phys*, 222, 2007.

[53] S. A. Ali, P. A. Gauglitz, and W. R. Rossen. Stability of Solids-Coated Liquid Layers between Bubbles. *Industrial & Engineering Chemistry Research*, 39(8), August 2000.

[54] D. J. Broesch and J. Frechette. From Concave to Convex: Capillary Bridges in Slit Pore Geometry. *Langmuir*, 28(44), November 2012.

[55] T. S. Horozov, R. Aveyard, J. H. Clint, and B. Neumann. Particle Zips: Vertical Emulsion Films with Particle Monolayers at Their Surfaces. *Langmuir*, 21(6), March 2005.

[56] E. P. Lewandowski, M. Cavallaro, L. Botto, J. C. Bernate, V. Garbin, and K. J. Stebe. Orientation and Self-Assembly of Cylindrical Particles by Anisotropic Capillary Interactions. *Langmuir*, 26(19), October 2010.

[57] G. D. M. Morris, S. J. Neethling, and J. J. Cilliers. A Model for the Stability of Films Stabilized by Randomly Packed Spherical Particles. *Langmuir*, 27(18), September 2011.